Environmental Research 247 (2024) 118120

Contents lists available at ScienceDirect

Environmental Research

journal homepage: www.elsevier.com/locate/envres

Green synthesis of $BiVO_4$/Eco-graphene nanostructures for the elimination of sulfamethoxazole by adsorption and photo-degradation using blue LED light

A.I. Moral-Rodríguez *, L.D. Ramírez-Valencia, E. Bailón-García, F. Carrasco-Marín, A.F. Pérez-Cadenas **

UGR-Carbon - Materiales Polifuncionales Basados en Carbono, Dpto. Química Inorgánica - Unidad de Excelencia Química Aplicada a Biomedicina y Medioambiente - Universidad de Granada, ES18071, Granada, Spain

ARTICLE INFO

Keywords:
Eco-graphene
$BiVO_4$
Photocatalysis
LED light
Sulfamethoxazole
Emerging contaminants

ABSTRACT

Photo-catalysts based on $BiVO_4$ (BV) and Eco-graphene (EG) were synthesized and obtained in a single step with high-quality properties. These nanostructures (NEs) were obtained through a green chemistry route and by adding 2, 3, and 5 wt% of a homemade EG. The BV/X EG NEs (where X = corresponds to the weight % of EG) demonstrated high photocatalytic activity, obtaining Sulfamethoxazole degradation percentages of 40, 45, 52, and 57 for BV, BV/2 EG, BV/3 EG, and BV/5 EG respectively, using a blue LED light. In addition, it was observed that the presence of EG slightly affected the surface area and porosity of BV. Moreover, it was observed that the presence of EG stabilized the scheelite monoclinic phase (*m-s*), and decreased the crystal size and band-gap values of BV-based samples. It was detected that EG contents increased the BV reduction, creating oxygen vacancies and V^{4+} states, which favored electron transfer, enhanced the photo-catalytic activity, and decreased the recombination rate. The adsorption influence of the BV/EG system was also studied. Finally, the stability tests of these materials after four cycles of reuse allowed keeping practically the full degradation capacity, demonstrating that these NEs represent a promising material driven by visible light that can be used for wastewater decontamination in the presence of drugs.

1. Introduction

Currently, it is roughly calculated that 80 % of the world's wastewater is returned untreated to ecosystems (United Nations, 2017), resulting in the deposition of contaminated load in waters which poses a serious risk to ecosystems. Emerging contaminants (ECs) are unrecognized or unregulated chemical compounds, which are continuously being incorporated into air, water, or soil. Continued biological exposure of ECs, even at low levels of exposure, might affect the aquatic life, provoking environmental imbalances in all levels including the reproduction rate of species (Quadra et al., 2016). Pharmaceuticals are one of the most detected ECs in wastewater. In Latin America, some reports have confirmed the presence of drugs in water. Peña-Guzmán et al. (2019) determined a total of 51 ECs in wastewater analyses; Ecuador was the country with the highest number of cases (11), Mexico (7), Brazil and Colombia (3) and Argentina and Venezuela (1). Some of the drugs detected mainly in wastewater from Ecuador and Mexico were trimethoprim, naproxen, ibuprofen, sulfamethoxazole, carbamazepine and caffeine (Peña-Guzmán et al., 2019). The presence of sulfonamides, tetracyclines and trimethoprim has been detected in aquatic environments in countries such as China, France, Germany, Greece, India, Portugal, and Spain (Afonso-Olivares et al., 2017; Ben et al., 2018; Mailler et al., 2015; Santos et al., 2013; Subedi et al., 2017; Thomaidis et al., 2016; Vergili et al., 2019).

According to WHO classification J01E, Sulfamethoxazole (SMX) in combination with Trimethoprim is currently the fourth most widely used antibiotic in the world, after penicillin's, macrolides and fluoroquinolones (Van Boeckel et al., 2014). SMX is an antibiotic of the sulfonamide group that is widely prescribed in the treatment of respiratory or urinary tract infections (Sarker et al., 2023). In recent years, its presence in high concentrations has been detected in wastewater effluents from the pharmaceutical industry in South Korea (Sim et al., 2011)

* Corresponding author.
** Corresponding author.
E-mail addresses: aimr17@correo.ugr.es (A.I. Moral-Rodríguez), afperez@ugr.es (A.F. Pérez-Cadenas).

https://doi.org/10.1016/j.envres.2024.118120
Received 28 September 2023; Received in revised form 29 December 2023; Accepted 4 January 2024
Available online 8 January 2024

(166 μg L^{-1}), domestic in South Africa (59.28 μg L^{-1}) (Matongo et al., 2015) and municipal in the USA (113.6 μg L^{-1}) (Oliveira et al., 2015). SMX concentrations in water have the potential to affect bacterial cycles, essential for the development of aquatic ecology, induce resistant genes in microorganisms, and cause damages to human health (de Jesus Gaffney et al., 2015). Therefore, there is a great necessity to remove this antibiotic from conventional water treatment processes.

Photo-catalytic oxidation emerges as an alternative chemical process, effective for wastewater decontamination and able to degrade a broad amount of organic pollutants (Koe et al., 2019). Photo-catalytic oxidation can work using solar radiation as a renewable and naturally available energy source, and in turn, making possible sustainable processes and/or green ones (Byrne et al., 2018). Some metal oxides, such as TiO_2, have been extensively investigated. Unfortunately, and due to its high energy bandgap (E_g) of 3.2 eV, TiO_2 can only be excited by UV radiation, which occupies only 4 % of the spectrum of sunlight entering the Earth (Wang et al., 2014).

Bismuth-based semiconductor (SC) materials have garnered considerable attention, due to their good solar light absorption, high catalytic activity, abundance, and low price (Cho et al., 2015). $BiVO_4$ (BV) is a very promising n-type SC due to its photoactivity in the region between 400 and 700 nm, high chemical stability, non-toxicity and low cost (Malathi et al., 2018). The catalytic activity of BV is strongly dependent on the crystal shape. BV has three polymorphs: tetragonal zircon (*t*-z), and monoclinic (*m*-s) or tetragonal scheelites (*t*-s). According to the literature the E_g of *t-z, m-s* and *t-s* phases are 2.34, 2.40 and 2.90 eV, respectively (Li et al., 2012). Thus, the *m-s* phase has become an ideal photocatalyst that allows it to absorb in the visible region (Xie et al., 2014). Nonetheless, BV exhibits an electron-hole pair recombination rate large, which limits the photodegradation efficiency and a low adsorption capacity (Malathi et al., 2018). Therefore, different methods have been implemented to improve these limitations of the BV (Munir Sajid et al., 2023). For example, the preparation of semiconductors based in a heterojunction and the design of a texture by doping with transition metals or non-metal ions (Chakhtouna et al., 2021; Liu et al., 2023; Zhai et al., 2020). On the other hand, graphene (G) as a carbonaceous material, made up of sp^2 hybrid carbon atoms only one atom thick, possesses several properties such as electron mobility, a narrow E_g, large surface area values and good mechanical strength (Zhang et al., 2012). However, G-sheets commonly present problems of agglomeration and restacking during use, leading to loss of effective surface area and consequently the decrease of the adsorption capacity (Baaziz et al., 2014). An efficient way in order to prevent the re-stacking of films, is the docking of multifunctional metal or oxide nanostructures (NEs) or nanoparticles (NPs), e.g., Bi-based (Bi-NPs), which further derives in the preparation of bi-functional NEs, based on an adsorbent and photocatalyst material with superior photo-catalytic properties (Zhang et al., 2016).

The photo-catalytic efficiency for BV catalysts depends strongly on the properties such as crystal structure, morphology and band energy structure (Sajid et al., 2021). Therefore, the synthesis method is very important in obtaining NEs (Malathi et al., 2018). The synthesis of inorganic NEs through green chemistry methodologies or routes, limits the use of hazardous reagents, solvents, toxic by-products, reduction in the synthesis stages, among others (Mao et al., 2007; Sajid et al., 2020). The synthesis of BV/G as a hybrid nanostructure has obtained excellent results in applications related to energy storage (Dutta et al., 2018), hydrogen and oxygen production by photochemical water splitting (Ng et al., 2010) and in the photodegradation of pollutants (Yan et al., 2013).

Until now, these materials have been obtained in environmentally unfriendly ways. In some of these works, the added G is obtained by synthetic chemical methods such as Brodie's or Hummers' method (Brodie, 1860; Hummers and Offeman, 1958). The G obtained by Brodie's method mainly uses graphite, fuming HNO_3 and $KClO_3$. However, during synthesis, there is a release of noxious gases such as NOx and ClO_2, and explosion hazards caused by the decomposition of ClO_2 at a temperature >45 °C (Eigler, 2016). On the other hand, obtaining G by the Hummer's method from graphite, $KMnO_4$, and $NaNO_3$ in H_2SO_4 can similarly cause an explosion risk as Mn_2O_7 decomposes at a temperature >55 °C (Eigler, 2016). Moreover, the generated hazardous waste materials require treatment, resulting in additional production costs and a serious environmental impact. Although efforts have been made to optimize the synthesis of G, it still requires toxic chemical reagents, very long reaction times, and instability of the chemical reagents (Wang et al., 2021).

The obtaining of Eco-graphene (EG), from the cyclic polymerization of glucose and through a hydrothermal route, represents a novel one-step, simple, and environmental friendly strategy, which allows the production of carbon materials with tuned functional properties that can be used as support materials in the synthesis of photocatalysts (Mohamed et al., 2020). The synthesis of EG minimizes the use of toxic chemical reagents and is a viable option to replace traditional methods in obtaining G.

In this work, we presented the synthesis of BV/EG nanostructures by green chemistry routes, as well as their application in the adsorption and photo-degradation of SMX using visible light. The BV/EG NEs were synthesized at different %wt. of EG by hydrothermal method. The structure, physico-chemical properties, the adsorption capacity and the photo-catalytic activity were analyzed to evaluate the role of EG in the improvement of their photo-catalytic performance.

2. Material and methods

2.1. Synthesis of eco-graphene

The eco-friendly synthesis of EG was carried out starting by the hydrolysis of glucose in ammonia/CTAB media, followed by a hydrothermal process. For the synthesis, CTAB was dissolved in a 0.5 M solution of glucose, fixing a molar ratio of CTAB/glucose as 1.5/8. Then, ammonium hydroxide was incorporated to the above-mentioned solution, fixing 1/10 volumetric ratio and reaching a pH of 11. The final solution was treated in an autoclave at 270 °C for 4 h. After a slow cooling to room temperature, the product obtained was collected by filtration, washed using distilled water, and dried at 70 °C under vacuum for two days.

2.2. Synthesis of BV/EG photocatalysts

These materials were prepared by a hydrothermal synthesis route consisting of dissolving 1 mmol of bismuth (III) nitrate pentahydrate in 20 mL of nitric acid 1M, and 1 mmol of ammonium vanadate (V) in 20 mL of sodium hydroxide 0.5 M. The solution of ammonium vanadate (V) was added carefully to the bismuth (III) nitrate pentahydrate solution, until a clear and yellow solution was obtained. Then the pH of the solution was fixed to 2 using sodium hydroxide (3 M). After that, for the EG-containing photo-catalyst, the corresponding amount in wt.% of EG was added. The mixed solution was stirred for 20 min at room temperature and subjected to ultrasound for 15 min. Subsequently, this last solution was transferred to a 100 mL Teflon-lined stainless-steel autoclave, hermetically sealed, and treated at 140 °C for 12 h. After cooling, the obtained samples were washed three times with deionized water, and once with ethanol. Finally, the particles were dried at a temperature of 80 °C for 12 h. The photo-catalysts were denoted BV and those containing EG were denoted BV/X EG (where X = corresponds to the wt.% EG). The percentages by weight of EG used were 2, 3 and 5.

2.3. Photocatalyst characterization

The surface area, pore-volume and the pore diameter of the BV/EG NEs were analyzed using an N_2 physisorption equipment, Micromeritics, ASAP 2420. The Brunauer-Emmett-Teller method was used in order to determine the apparent surface area (S_{BET}) and the total pore volume at

$P/P_0 \approx 0.99$ (Brunauer et al., 1938). XRD patterns of the photo-catalysts were done on a Bruker D8 Discover diffractometer using Cu Kα radiation (λ = 1.5406 Å) in the range of 10 to 80º (2θ) with a scan rate of 0.02 °/s and voltage of 50 KV. Raman spectra were obtained on a JASCO NRS-5100 dispersive Micro-Raman spectrometer, using a 532 nm laser as excitation source, in a range from 100 to 1000 cm^{-1}. The crystallite size (d_{XRD}) was obtained using the Scherrer equation (Holzwarth and Gibson, 2011). For diffuse reflectance and UV–Vis absorbance analyses a UV–Vis spectrophotometer, brand VARIAN CARY-5E was used. The E_g of the photo-catalysts were calculated using the Kubelka-Munk $(F(R)\text{-}E)^{1/2}$ method (Kubelka, 1948; Yang and Kruse, 2004). TEM analyses were carried out on a Carl Zeiss SMT LIBRA 120 Plus microscope. The composition of the surface chemistry of BV/EG NEs was studied by X-ray photoelectron spectroscopy (XPS) with a Kratos Axis Ultra-DLD equipment. The point zero charge (pH_{PZC}) of the photo-catalysts was obtained by the pH variation method (Lopez-Ramon et al., 1999).

2.4. Adsorption tests

The SMX adsorption kinetic on the photo-catalysts was studied to know the time required to obtain the adsorption equilibrium in the darkness. At the beginning of these experiments, the pH was adjusted to 7 with solutions of 0.01 N of NaOH and HCl. Then, 150 mg of each photocatalyst was placed in contact with 150 mL of SMX solution with an initial concentration (5 mg L^{-1}) in a flask. Then, the flask was placed in in a thermostatic bath with a continuous stirrer fixing the temperature of the solution. Aliquots were taken at different times from the flask and these were used to determine the final concentration of SMX previous filtration. The concentration of SMX was analyzed using a UV–Vis spectrophotometer at 264 nm (Jeanway 6505). The adsorption kinetic indicated that the required time to reach the adsorption equilibrium and the saturation is 4 h, depending of the material used. The SMX adsorption isotherms on BV/EG system were performed in the same conditions, using 25 mg of the photocatalyst placed in 25 mL of a solution of initial concentration of SMX ranging from 1 to 30 mg L^{-1}. The solutions were placed inside the thermostatic bath under continuous stirring for 4 h, to assure the equilibrium of adsorption. Once the experiments reached equilibrium, 1 mL of sample was filtered and the concentration of SMX measured by UV–Vis spectrometry. The adsorption of XMS on the BV samples was calculated by equation (1):

$$q = \frac{V(C_0\text{-}C_e)}{m} \quad (1)$$

where q is the adsorbed amount (mg g^{-1}), V is the volume of the solution (L), C_0 is the initial concentration of the solution of SMX (mg L^{-1}), C_e is the concentration of SMX at equilibrium (mg L^{-1}) and m is the amount of adsorbent (g). Freundlich and Linear adsorption models were applied to the experimental adsorption data of SMX on BV and BV/EG. The isotherms can be expressed mathematically as follows:

$$q = kC_e^{1/n} \quad (2)$$

$$q = aC \quad (3)$$

where k is the Freundlich constant ($mg^{1\text{-}1/n}\ L^{1/n/g}$); n is the dimensionless Freundlich isotherm constant; a (L g^{-1}) is the isotherm constant of the Linear model and is obtained by simplifying the Radke-Prausnitz isotherm where b = 0. The parameters of the isotherm models were estimated by adjusting the Freundlich and linear isotherm model to the experimental values by a non-linear-squares method based on the Rosenbrock-Newton algorithm. The average absolute percentage variation (%D), was calculated by the following equation:

$$\%D = \left(\frac{1}{N}\sum_{i=1}^{N}\left|\frac{q_{exp}\text{-}q_{cal}}{q_{exp}}\right|\right) \times 100\ \% \quad (4)$$

where N is the number of experimental data values; q_{exp} is the experimental mass of SMX adsorbed on BV and BV/EG (mg g^{-1}); and q_{cal} is the mass of SMX adsorbed predicted with the adsorption isotherm. The isotherm parameters and the % D are shown in Table 2.

2.5. Photo-catalytic tests

The photodegradation performance of system BV/X EG (where X = corresponds to the wt.% EG) was tested in the SMX degradation using a borosilicate glass reactor at a irradiation distance of 3 cm. SMX photocatalytic test were carried out under visible light irradiation, using high-power LEDs (465 nm main emission, total electric power ~ 68 W and 4080 lumen/W). The pH of the experiments at the beginning, was adjusted to 7 with different solutions of NaCl and HCl (0.01 N), and during the kinetic the temperature was maintained at 30 °C.

The photo-catalyst was added to 100 mL of SMX solution (5 mg L^{-1}) and dispersed by sonication. Then the suspensions were stirred at 500 rpm for 4 h in the darkness before exposure to irradiation, in order to reach the corresponding equilibrium. Afterward, 1.5 mL were sampled to extract only 10 % of volume total. Then the aliquots were filtered and the SMX concentration was analyzed with a UV–Vis 6505 JENWAY Spectrophotometer by registering the SMX maximum absorption at the wavelength of 260 nm.

The SMX photodegradation kinetics were studied using the following first and second order kinetic model equations (5) and (6):

$$[C]_f = [C]_0 e^{-k_1 t} \quad (5)$$

$$\frac{1}{[C]_f} = k_2 t + \frac{1}{[C]_0} \quad (6)$$

$[C]_f$ and $[C]_0$ represent the concentration of SMX (mg L^{-1}) at t (min) and t = 0, respectively. k_1 (min^{-1}) and k_2 (L mg^{-1} min^{-1}) are the first and second-order reaction rate constants, respectively, which were obtained by a non-linear-squares method based on the Rosenbrock-Newton algorithm.

SMX mineralization was performed through the measurement of TC and TOC, using a Shimadzu model V-CSH analyzer. Toxicity tests of solutions were carried out using the normalized biotest (UNE/EN/ISO 11345-2) of luminescent inhibition of *Vibrio Fischeri* bacteria, before and after photo-catalytic kinetic, and using the LUMIStox 300 System (Dr. LangeGmbH) with a LUMIStherm incubator. Toxicity was evaluated as inhibition percentages at 15 min of exposure (I_{15}) and referred to a stock saline solution as control.

3. Results and discussion

The N_2 adsorption-desorption isotherms are shown in Fig. 1 As can be seen in this figure, the samples present a type II isotherm, typically of non-porous or microporous materials.

Furthermore, according to the results shown in Table 1, the S_{BET} and V_p values of BV/EG Nes, increased slightly with the addition of EG to BV. The addition of EG during BV synthesis may provide a larger number of active sites that can favor adsorption and photo-catalytic activity.

The structure and crystallinity of samples were studied by powder XRD measurements. The XRD patterns of BV/EG system with different content of EG, are shown in Fig. 2. It was noticed that the monoclinic scheelite (*m*-s) (JCPDS No. 00-075-1866) and tetragonal zircon (*t*-z) (JCPDS No. 00-014-0133) phases were detected in all samples. The diffraction peaks at 18.6°, 28.8°, and 30.5° correspond to (101), (121), and (040) crystal planes of *m*-s. While the peaks at 24.4° and 32.7° correspond to (200) and (112) crystal planes to the phase *t*-z. Fig. 2 does not show the presence of the main EG peak in the BV/EG Nes. This can be due to the low percentages of EG and good dispersion of EG on the surface of BV Nes. Even though in all samples a mixture of *m-s* and *t-z* is detected, note that the diffractogram of pure BV is quite different of the

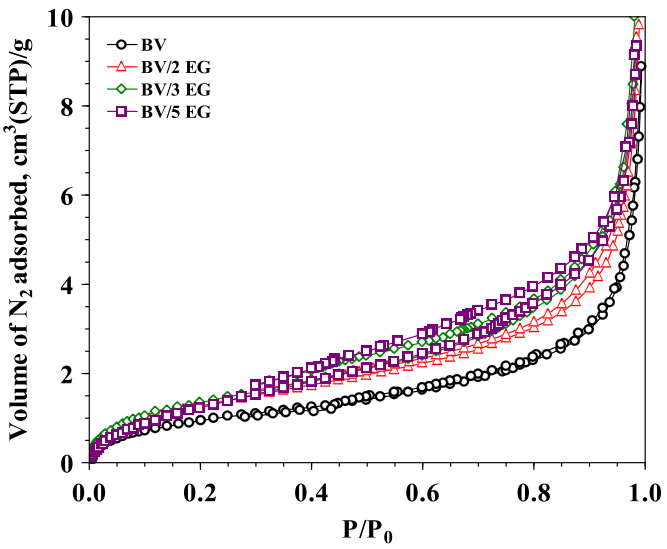

Fig. 1. N_2 adsorption-desorption isotherms of photo-catalysts.

BV/EG NEs one. Well-developed and intense peaks are observed for BV sample at 24.4° attributed to tetragonal phase, whereas this peak is much less intense for BV/EG NEs denoting a main stabilization of *m-s* crystalline phase by the presence of EG.

For further details, the percentage of the *m*-s phase was calculated by normalizing the intensities of the characteristic peak of the *m*-s phase (121) versus the characteristic peak of the *t*-z phase (200) using the following equation:

$$\eta_{mono} = \frac{I_{mono\ (121)}}{I_{mono(121)} + I_{tetra(200)}} \times 100 \quad (7)$$

where η_{mono} is the percentage of the monoclinic phase, $I_{mono\ (121)}$ and $I_{tetra\ (200)}$ are the principal peak characteristics of the monoclinic and tetragonal phases. The results indicated that the *m*-s phase is the one found in a higher proportion, concerning to the *t*-z phase. Nonetheless, it is important to highlight that the presence of EG during the synthesis, highly affects the crystalline phase stabilized. Around 60 % of monoclinic phase is obtained in pure BV, whereas this proportion highly increases up to around 90 % in BV/EG NEs. Moreover, the crystal size (d_{XRD}) seems also to be affected by the presence of EG. The d_{XRD} of BV is 29.9 nm, whereas this value decreases in BV/EG Nes, ranging from 20.3 to 18.3 nm (Table 1); particle size decreased with the addition of EG content, with the BV/5 EG photocatalyst being the NE with the smallest d_{XRD} size (Table 1). This reduction in crystal size and the stabilization of the *m-s* crystalline phase may favor the photo-catalytic activity of the NE. Several authors have pointed out that *m-s* BV is the most photo-catalytically active phase over the other crystal forms (Fan et al., 2012; Tokunaga et al., 2001)

Fig. 1S. shows the Raman spectra of BV/EG NEs in the range of 250–1000 cm^{-1} (a) and 1000 to 2000 cm^{-1} (b). The modes observed at 336 and 370 cm^{-1} correspond to antisymmetric and symmetric (VO_4^{3-}) bending vibrational modes, respectively. The mode at 809 cm^{-1} can be attributed to the stretching mode of the V–O bonds in the VO_4^{3-} tetrahedron of the crystal structure. In Fig. 1S, peaks are observed at 1363 and 1584 cm^{-1}, corresponding to the G and D bands of the EG. However, in the NEs at 2, 3, and 5 % by weight of EG, the D band is not visible in the Raman spectra, this might be due to the low percentages of EG added in the NEs. On the other hand, the G band of the NEs shows a blue shift at 1592 cm^{-1} compared to the starting EG. This shift may be due to the coverage of the BV by the EG after the hydrothermal synthesis process.

Fig. 3a shows the UV–Vis diffuse reflectance spectrum and (b) the determination of E_g values of the photocatalyst system. The samples showed a strong and intense absorption from UV to visible light region,

Table 2
Kinetic parameters and average percentage deviation (%D) for the photo-degradation of SMX by BV/EG NEs.

Photo-catalyst	$k_1 \times 10^3$ (min^{-1})	%D	$k_2 \times 10^3$ (L mg^{-1} min^{-1})	%D
BV	1.06	1.46	1.31	1.33
BV/2 EG	1.30	3.15	1.73	1.58
BV/3 EG	1.55	4.80	2.05	2.25
BV/5 EG	1.76	5.10	2.48	1.78

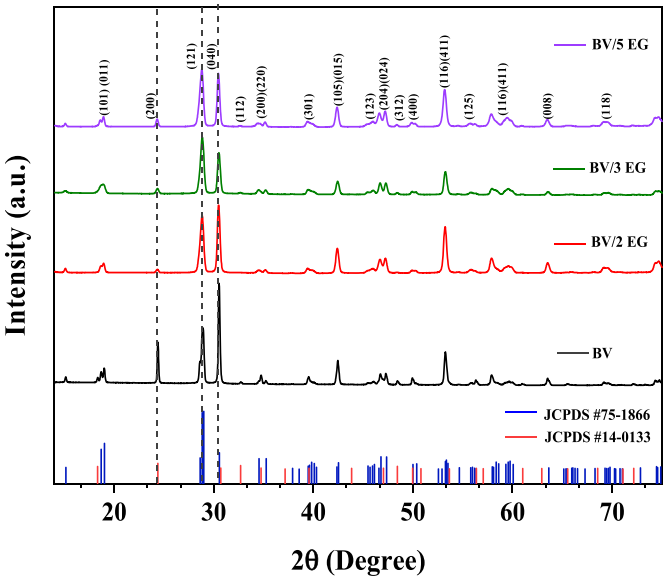

Fig. 2. XRD spectra of samples: BV, BV/2 EG, BV/3 EG and BV/5 EG.

Table 1
Textural properties of the system BV/EG.

Photocatalyst	S_{BET}[a] (m^2 g^{-1})	V_p[b] (cm^3 g^{-1})	D_p[c] (nm)	η_{mono}[d] (%)	d_{XRD}[e] (nm)	E_g[f] (eV)	pH_{PZC}[g]
BV	3.5	0.014	15.9	57.2	29.9	2.43	4.2
BV/2 EG	4.7	0.019	16.0	93.7	20.3	2.42	4.8
BV/3 EG	5.0	0.020	16.2	90.0	19.0	2.42	4.8
BV/5 EG	4.9	0.019	15.6	88.0	18.3	2.40	4.9
EG	0.6	0.002	14.6	–	–	–	4.5

[a] Surface area (S_{BET}).
[b] Total pore volume was determined at $P/P^0 \approx 0.99$.
[c] Average pore diameter (D_p).
[d] Percentage of monoclinic phase (η_{mono}).
[e] Crystal size (d_{XRD}).
[f] Value of band-gap (E_g).
[g] pH point zero charge (pH_{PZC}).

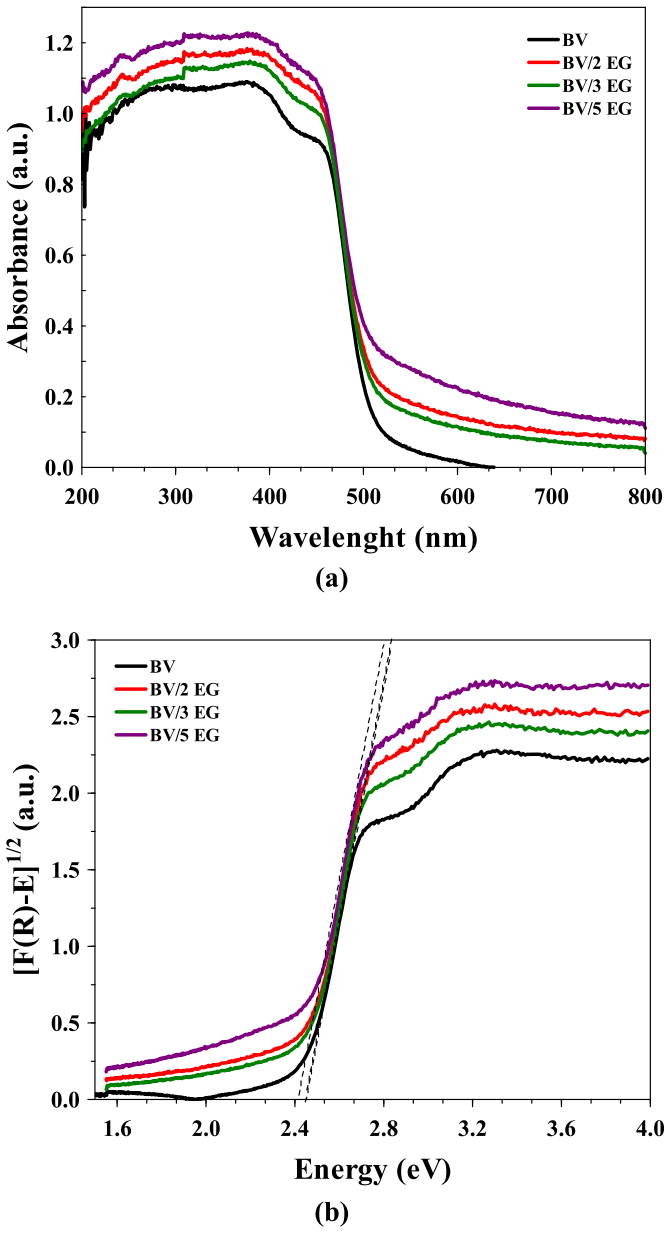

Fig. 3. UV–Vis diffuse absorbance spectra (a) and the E_g (b) of the BV/EG NEs.

indicating that the photo-catalysts could be active under sunlight with the introduction of EG, and at the same time have a positive effect on the optical properties. The calculated band gaps for BV, BV/2 EG, BV/3 EG, and BV/5 EG were 2.43 (BV), 2.42 (BV/2 EG), 2.42 (BV/3 EG), and 2.40 eV (BV/5 EG). After the addition of EG to BV, the adsorption of light of $\lambda > 500$ nm increases, and the E_g values decrease slightly. The difference may be related to the structure and crystallinity of each photocatalyst, such as the crystallite size and the presence of EG in a higher weight percentage. BV/5 EG showed the lowest E_g value, which could lead to higher photo-catalytic activity and effective photogenerated electron transfer of the BV/EG system.

The microstructure of the system BV with different loading EG was characterized using transmission electron microscopy (TEM) and results are shown in Fig. 4. Fig. 4(a–d) exhibits agglomerates of irregular plate-like particles with heterogeneous sizes of particles. After the incorporation of the EG, the flakes covered the BV particles, and the contact of BV with EG can be noted (Fig. 4 b-d). These results confirm that the photo-catalysts binary were possibly obtained.

The Infrared Spectra of the synthesized BV/EG photo-catalysts are shown in Fig. 2S. In the spectrum, the main bands in EG sample are located at 2982, 2910, 1588, 1408, and 1063 cm^{-1}, corresponding to the O–H stretching, C=C in-plane, N–CH_3 stretching, and epoxy C–O–C vibrations (Mohamed et al., 2020), respectively. In BV/EG NEs, new intense bands are also observed at 1080, 631 and 478 cm^{-1}, which are assigned to V=O stretching vibration, VO_4^{3-} bending mode and Bi–O stretching vibration (Ghani et al., 2020), correspondingly.

The pH_{PZC} is an important value for determining the interaction that can occur between the surface charge of a photocatalyst and an organic compound. Thus, for the BV system, the surface is positively charged below pH_{PZC} and negatively charged above the pH_{PZC}. The pH_{PZC} was obtained for BV/EG system and the results are shown in Table 1. The results indicated that BV and BV/EG has a pH_{PZC} acid, which can be attributed to the presence of oxygenated groups derived from the synthesis of EG (Mohamed et al., 2020).

The chemical nature of the sample surface was also studied by XPS. High resolution regions are depicted in Fig. 5. The deconvolution of Bi_{4f} spectra (Fig. 5a) reveals a doublet at 158.1 and 163.6 eV, with an orbital splitting of 5.5 eV that is ascribed to the $Bi_{4f7/2}$ and $Bi_{4f5/2}$ lines of Bi^{+3} (Kamble and Ling, 2020; Regmi et al., 2018).

Fig. 5b shows the deconvolution of V_{2p} spectral region. The peak at 517.0 eV correspond to V^{5+} in BV. Note that for BV/EG the peaks are displaced around 0.8 eV to higher binding energy regarding BV sample, denoting an electron deficient environment in these samples, which could be attributed to an electronic transfer from BV to EG. The peak at 515.8 eV in BV sample is indicative to the presence of a small amount of V^{4+} species. This peak increases by increasing the amount of EG in the samples, indicating that BV/EG samples are oxygen deficient and the amount of non-stoichiometric oxygen/oxygen vacancies at the surface is dependent on the EG content, which can be advantageous for the enhancement of photo-catalytic behavior.

In order to fit the O_{1s} region in BV sample, two peaks have been required at 529.2 eV and 531.7 eV, which have been assigned to total oxygen atoms in the stoichiometric form, and superficial oxygen forming functional groups, mainly hydroxyl (−OH) groups, respectively. Nonetheless, four components are required to fit this spectral region of BV/EG samples, as a consequence of the different V-species and the oxygen linked to the carbon phase. Thus, the components at 529 and 530 eV binding energies can be ascribed to the lattice oxygen of BV structure and oxygen vacancies formed on the surface, whereas the peaks at 531.6 and 533.0 eV correspond to C=O and C–O bonds of the oxygenated surface groups of the carbon phase (Stathi et al., 2021). It is important to highlight that again, a shift of peaks is observed in BV/EG samples regarding BV samples, denoting an electronic transfer from BV to EG and the lattice oxygen/oxygen vacancies ratio depend on the EG content of the samples. Overall, the presence of EG on the samples enhances the reduction of BV samples, creating oxygen vacancies and favoring the electron transfers from the BV to the EG, which can be advantageous for the enhancement of photo-catalytic behavior.

The adsorption capacity of BV and BV/EG to SMX from aqueous solution is shown in Fig. 3S. The values of isotherm constants and %D are shown in Table 1S. According to the values in Tables 1S and it is observed that although both models fitted the experimental data, the Freundlich model gave the lowest %D value.

In Fig. 3S, it is observed that the adsorption capacity of BV/2 EG, BV/3 EG, and BV/5 EG was lower than that the one obtained with BV. According to the speciation diagram (Fig. 4S), at pH 7 the SMX molecule presents a neutral charge, while BV and the BV/EG system have a positive surface charge. Therefore, electrostatic interactions are not determinant during the adsorption of SMX.

Since the adsorption capacity is low for BV and BV/EG photo-catalysts, the samples were saturated for 2 h in the dark to avoid taking the adsorption contribution in the photodegradation process. Once the adsorption equilibrium was reached, the LEDs were turned on, to irradiate the suspension and initiate the SMX photodegradation process. The dimensionless SMX concentration decay curves (C/C_0) are plotted in

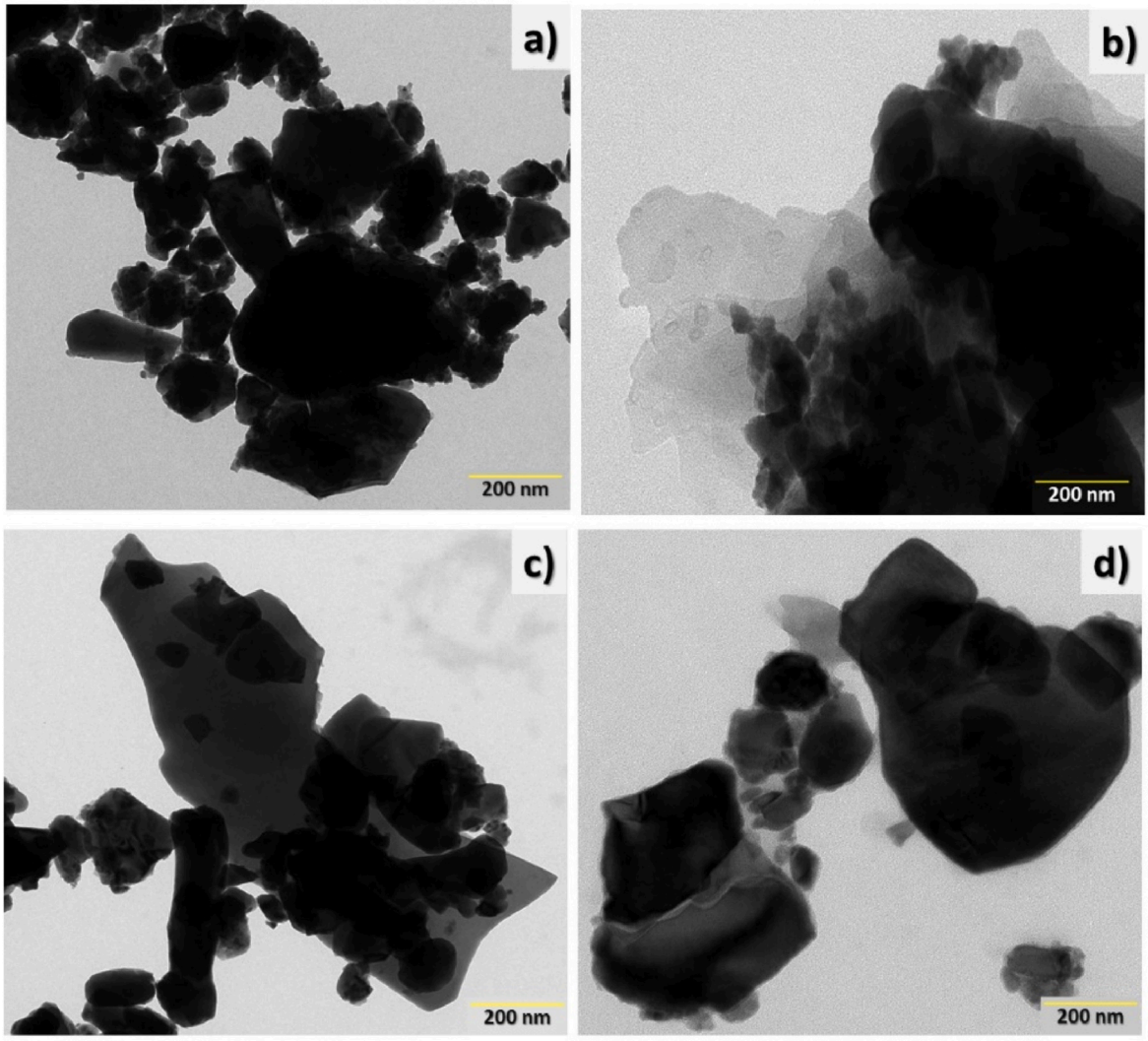

Fig. 4. TEM of a) BV, b) BV/2 EG, c) BV/3 EG, and d) BV/5 EG.

Fig. 6. A test designated as SMX_0, which consisted of irradiating the drug solution without photocatalyst, was performed to show the non-photolysis of the SMX molecule under irradiation conditions. The results showed that the photolysis of the SMX molecule can be neglected. As can be seen in Fig. 6, the percentage degradation of SMX obtained was 40, 45, 52, and 57 % for BV, BV/2 EG, BV/3 EG, and BV/5 EG catalysts, respectively. The incorporation of 2–5 wt% of EG into the Bi NEs shows an improvement in the photo-catalytic activity compared to the BV sample. Fig. 6S shows the correlation of the percentage of degradation of SMX vs the wt.% of EG. The results revealed that the percentage of degradation of SMX increased approximately linearly with increasing wt.% of EG.

Table 2 shows the obtained values of kinetic parameters and %D in the photo-degradation of SMX. As can be seen in Table 2, the %D values were lower when fitting the experimental data to the second-order kinetic model. Likewise, it was found that BV/5 EG obtained the best photo-catalytic activity. When comparing the k_2 values, it was observed that the photodegradation rate of BV/5 EG increased 1.89 times concerning BV. The photo-catalytic performance of the BV/2 EG, BV/3 EG, and BV/5 EG NEs is related to the interaction between the BV nanoparticles and the EG sheets during synthesis and E_g. As the EG content increased, the E_g value decreased due to the creation of oxygen vacancies and V^{4+} states, and the stabilization of the monoclinic phase was favored. Moreover, the presence of EG led to higher photo-catalytic activity, which may be due to its ability to decrease the recombination rate and increase the transfer of charge carriers (see XPS).

The reusability and recyclability of a photocatalyst after its first use, is an important point to evaluate in the efficiency of a photo-catalytic process. Therefore, Fig. 7 shows the SMX photodegradation kinetics, obtained with the BV/5 EG after four reuse cycles (4 cycles 8h). In this figure, it can be seen that the BV/5 EG photo-catalyst showed good photo-catalytic activity during the four cycles. In the first cycle, 57 % SMX degradation was obtained. However, after three reuse cycles, the % of degradation decreased slightly, being 55, 54.5, and 53.4 %, respectively. With these reusability tests, it can be assumed that BV/5 EG is a good candidate that can be used in the photo-degradation of SMX since its activity does not decrease noticeably after four reuse cycles. Table. 2S shows the TC and TOC values before and after the SMX photo-degradation process using BV/5 EG. According to these values, a mineralization percentage of 40.9 % was obtained after 8 h of irradiation. This TOC value indicated that mineralization is not easily achieved, which may be due to the generation of intermediates in the solution.

The degree of toxicity is an important factor to know the possible adverse effects that the presence of organic compounds can cause in aquatic species and ecosystems. Therefore, toxicity was determined concerning the degree of inhibition of *Vibrio Fischeri* bacteria. The bioluminescence of the bacterium *Vibrio Fischeri* decreases in the presence of contaminants, and it is expressed as a function of the %

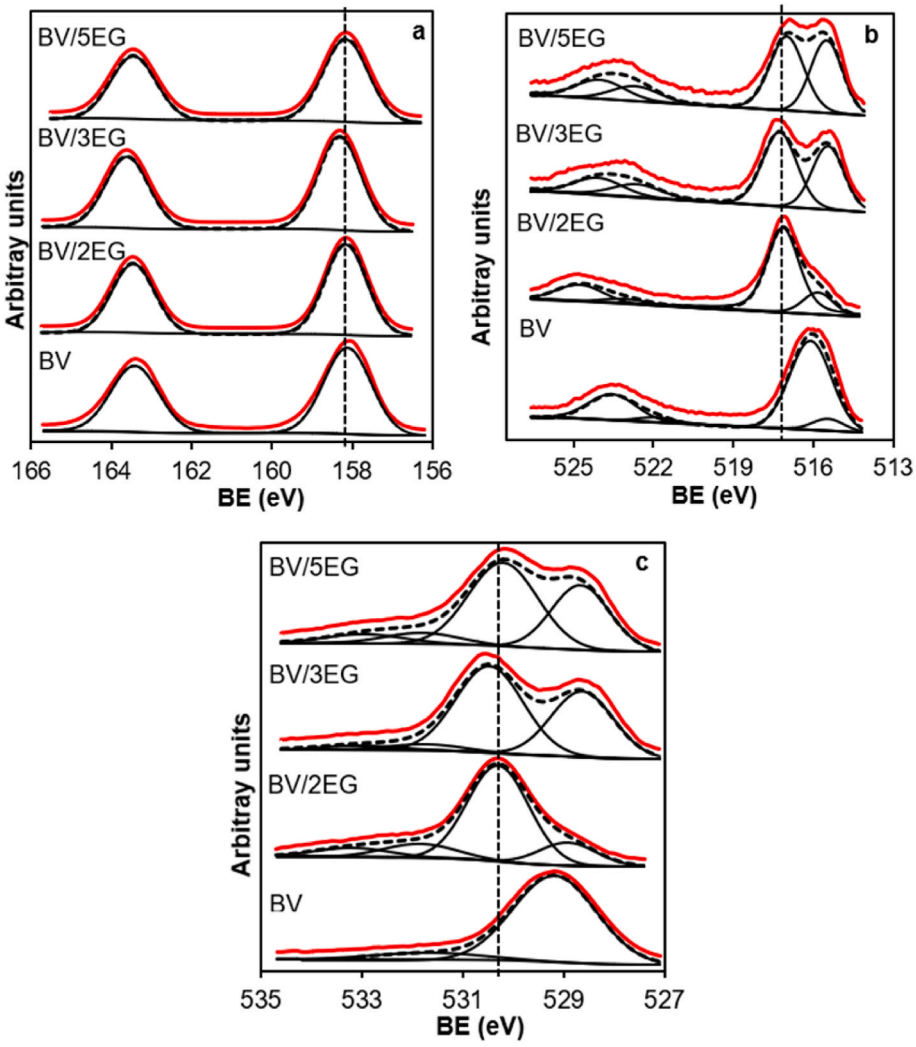

Fig. 5. XPS spectra of BV/EG samples, a) Bi4f, b) V2p and c) O1s regions.

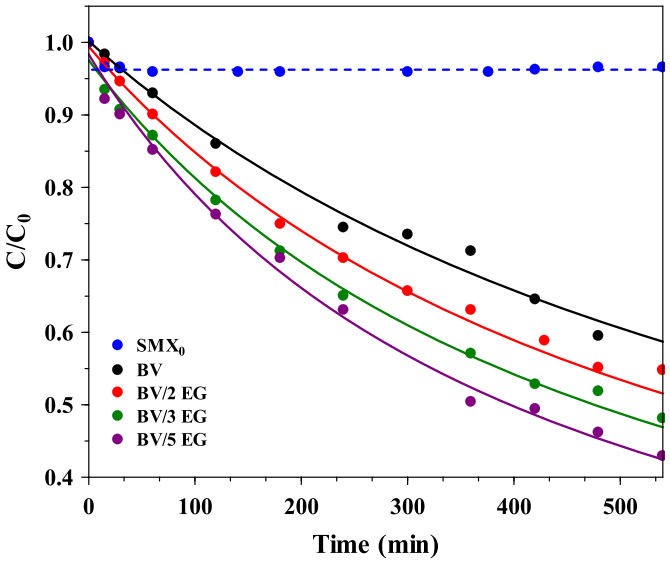

Fig. 6. Dimensionless concentration decay curves (C_A/C_{A0}) versus time (t = 0–540 min) for SMX degradation by BV/EG NEs.

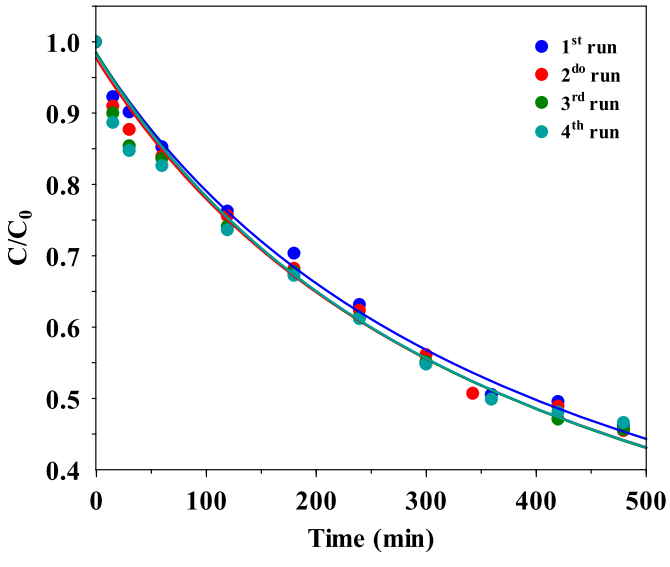

Fig. 7. Cycling experiments on the SMX photodegradation using BV/EG NEs.

inhibition of luminescence. As can be seen in Fig. 5S the % inhibition of bacterial bioluminescence before the photocatalysis process was 37.53 %. However, after 480 min of reaction, this value decreased by 25 %. This result, as well as the one obtained with the TOC determination, demonstrate that SMX degradation is not fully achieved. However, a reduction in the toxicity of the treated water in the presence of antibiotics such as SMX is achieved.

4. Conclusions

Photo-catalysts based on BV and EG were successfully synthesized via hydrothermal route, which were highly active under visible light for the SMX antibiotic degradation. These composites are based on nanostructured phases, part of them are a mixture of *m-s* and *t-z* phases. The presence of EG in the BV-based photo-catalysts stabilized the *m-s* crystalline phase, which is the most active, showing excellent photocatalytic performance. These materials contain band gaps around 2.4 eV, making them excellent sunlight-active photo-catalysts.

The adsorption of SMX on the photo-catalysts was low. However, the BV/EG series of NEs showed high photo-catalytic efficiency in the SMX degradation, especially those containing EG. This higher activity in the BV/EG composites may be related to the fact that the presence of EG improves the optical properties of the nanostructures, stabilizing the crystalline phase (*m-s*), promoting the reduction of BV-based photocatalysts with the creation of oxygen vacancies and V^{4+} oxidation states, which in turn favors the transfer of electrons from the vanadate phase to the EG, decreasing the recombination rate and increasing the transfer of charge carriers (as observed by XPs).

The BV/EG systems show notably higher activity compared to the starting BV ones under irradiation with blue LEDs. The composite with the maximum percentage of EG showed the best photo-catalytic performance reaching a 57 % of SMX degradation and high stability after four cycles of reuse. This type of photo-catalyst represents a promising, environmentally friendly, and cost-effective alternative to degrading pharmaceutical compounds in wastewater, using visible light.

CRediT authorship contribution statement

A.I. Moral-Rodríguez: Conceptualization, Data curation, Formal analysis, Investigation, Writing – original draft, Writing – review & editing. **L.D. Ramírez-Valencia:** Data curation, Investigation, Methodology. **E. Bailón-García:** Conceptualization, Formal analysis, Funding acquisition, Investigation, Project administration, Writing – original draft, Writing – review & editing. **F. Carrasco-Marín:** Funding acquisition, Investigation, Project administration, Resources, Supervision, Writing – review & editing. **A.F. Pérez-Cadenas:** Conceptualization, Funding acquisition, Investigation, Project administration, Writing – review & editing.

Declaration of competing interest

The authors declare that they have no known competing financial interests or personal relationships that could have appeared to influence the work reported in this paper.

Data availability

No data was used for the research described in the article.

Acknowledgements

This research has been supported by Junta de Andalucía (P18-RTJ-2974 and B.RNM.566.UGR20) projects and project PID2021-127803OB-I00 funded by MCIN/AEI/10.13039/501100011033/and by "ERDF A way of making Europe".

E. Bailón-García thanks the MICINN for a postdoctoral grant (RYC2020-029301-I). A. I Moral-Rodríguez thanks for the support of the postdoctoral research grant provided by the Consejo Nacional de Humanidades, Ciencias y Tecnologías (CONAHCYT, Mexico) through the Convocatoria de Estancias Posdoctorales en el Extranjero 2020. L.D. Ramírez-Valencia is grateful to the Colombian Ministry of Sciences, Technology and Innovation (MINCIENCIAS) for supporting her PhD studies. Funding for open access charge: Universidad de Granada / CBUA.

Appendix A. Supplementary data

Supplementary data to this article can be found online at https://doi.org/10.1016/j.envres.2024.118120.

References

Afonso-Olivares, C., Sosa-Ferrera, Z., Santana-Rodríguez, J.J., 2017. Occurrence and environmental impact of pharmaceutical residues from conventional and natural wastewater treatment plants in Gran Canaria (Spain). Sci. Total Environ. 599, 934–943. https://doi.org/10.1016/J.SCITOTENV.2017.05.058. –600.

Baaziz, W., Truong-Phuoc, L., Duong-Viet, C., Melinte, G., Janowska, I., Papaefthimiou, V., Ersen, O., Zafeiratos, S., Begin, D., Begin-Colin, S., Pham-Huu, C., 2014. Few layer graphene decorated with homogeneous magnetic Fe3O 4 nanoparticles with tunable covering densities. J. Mater. Chem. A 2, 2690–2700. https://doi.org/10.1039/C3TA14512C.

Ben, W., Zhu, B., Yuan, X., Zhang, Y., Yang, M., Qiang, Z., 2018. Occurrence, removal and risk of organic micropollutants in wastewater treatment plants across China: comparison of wastewater treatment processes. Water Res. 130, 38–46. https://doi.org/10.1016/J.WATRES.2017.11.057.

Brodie, B.C., 1860. II. On the atomic weight of graphite. Proc. Roy. Soc. Lond. 10, 11–12. https://doi.org/10.1098/RSPL.1859.0007.

Brunauer, S., Emmett, P.H., Teller, E., 1938. Adsorption of gases in multimolecular layers. J. Am. Chem. Soc. https://doi.org/10.1021/ja01269a023.

Byrne, C., Subramanian, G., Pillai, S.C., 2018. Recent advances in photocatalysis for environmental applications. J. Environ. Chem. Eng. 6, 3531–3555. https://doi.org/10.1016/J.JECE.2017.07.080.

Chakhtouna, H., Benzeid, H., Zari, N., Qaiss, A. el kacem, Bouhfid, R., 2021. Recent progress on Ag/TiO2 photocatalysts: photocatalytic and bactericidal behaviors. Environmental Science and Pollution Research 2021 28 (33 28), 44638–44666. https://doi.org/10.1007/S11356-021-14996-Y.

Cho, D.W., Cho, S.H., Song, H., Kwon, E.E., 2015. Carbon dioxide assisted sustainability enhancement of pyrolysis of waste biomass: a case study with spent coffee ground. Bioresour. Technol. 189, 1–6. https://doi.org/10.1016/J.BIORTECH.2015.04.002.

de Jesus Gaffney, V., Almeida, C.M.M., Rodrigues, A., Ferreira, E., Benoliel, M.J., Cardoso, V.V., 2015. Occurrence of pharmaceuticals in a water supply system and related human health risk assessment. Water Res. 72, 199–208. https://doi.org/10.1016/J.WATRES.2014.10.027.

Dutta, S., Pal, S., De, S., 2018. Hydrothermally synthesized BiVO4-reduced graphene oxide nanocomposite as a high performance supercapacitor electrode with excellent cycle stability. New J. Chem. 42, 10161–10166. https://doi.org/10.1039/C8NJ00859K.

Eigler, S., 2016. Controlled chemistry approach to the oxo-functionalization of graphene. Chem. Eur J. 22, 7012–7027. https://doi.org/10.1002/CHEM.201600174.

Fan, H., Jiang, T., Li, H., Wang, D., Wang, L., Zhai, J., He, D., Wang, P., Xie, T., 2012. Effect of BiVO 4 Crystalline Phases on the Photoinduced Carriers Behavior and Photocatalytic Activity. J. Phys. Chem. C 116, 22. https://doi.org/10.1021/jp206798d.

Ghani, N., Iqbal, J., Sadaf, S., Nawaz Bhatti, H., Asgher, M., 2020. Comparison of photo-esterification capability of bismuth vanadate with reduced graphene oxide bismuth vanadate (RGO/BiVO4) composite for biodiesel production from high free fatty acid containing non-edible oil. ChemistrySelect 5, 9245–9253. https://doi.org/10.1002/SLCT.202001913.

Holzwarth, U., Gibson, N., 2011. The Scherrer equation versus the "Debye-Scherrer equation.". Nature Nanotechnology 2011 6 (9 6). https://doi.org/10.1038/nnano.2011.145, 534–534.

Hummers, W.S., Offeman, R.E., 1958. Preparation of graphitic oxide. J. Am. Chem. Soc. 80, 1339. https://doi.org/10.1021/JA01539A017/ASSET/JA01539A017.FP.PNG_V03.

Kamble, G.S., Ling, Y.C., 2020. Solvothermal synthesis of facet-dependent BiVO4 photocatalyst with enhanced visible-light-driven photocatalytic degradation of organic pollutant: assessment of toxicity by zebrafish embryo. Scientific Reports 2020 10 (1 10), 1–11. https://doi.org/10.1038/s41598-020-69706-4.

Koe, W.S., Lee, J.W., Chong, W.C., Pang, Y.L., Sim, L.C., 2019. An overview of photocatalytic degradation: photocatalysts, mechanisms, and development of photocatalytic membrane. Environmental Science and Pollution Research 2019 27 (3 27), 2522–2565. https://doi.org/10.1007/S11356-019-07193-5.

Kubelka, P., 1948. New contributions to the optics of intensely light-scattering materials. J. Opt. Soc. Am. 38, 448–457. https://doi.org/10.1364/JOSA.38.000448.

Li, G., Bai, Y., Zhang, W.F., 2012. Difference in valence band top of BiVO 4 with different crystal structure. Mater. Chem. Phys. 136, 930–934. https://doi.org/10.1016/J.MATCHEMPHYS.2012.08.023.

Liu, Yulin, Zhu, Z., Liu, Yongqi, Wu, J., Ling, Y., Xiang, Z., Qin, S., Ye, Y., Bai, M., 2023. First principles insight on enhanced photocatalytic performance of sulfur-doped bismuth oxide iodate. Mater. Sci. Semicond. Process. 165, 107672 https://doi.org/10.1016/J.MSSP.2023.107672.

Lopez-Ramon, M.V., Stoeckli, F., Moreno-Castilla, C., Carrasco-Marin, F., 1999. On the characterization of acidic and basic surface sites on carbons by various techniques. Carbon 37, 1215–1221. https://doi.org/10.1016/S0008-6223(98)00317-0.

Mailler, R., Gasperi, J., Coquet, Y., Deshayes, S., Zedek, S., Cren-Olivé, C., Cartiser, N., Eudes, V., Bressy, A., Caupos, E., Moilleron, R., Chebbo, G., Rocher, V., 2015. Study of a large scale powdered activated carbon pilot: removals of a wide range of emerging and priority micropollutants from wastewater treatment plant effluents. Water Res. 72, 315–330. https://doi.org/10.1016/J.WATRES.2014.10.047.

Malathi, A., Madhavan, J., Ashokkumar, M., Arunachalam, P., 2018. A review on BiVO4 photocatalyst: activity enhancement methods for solar photocatalytic applications. Appl. Catal. Gen. 555, 47–74. https://doi.org/10.1016/J.APCATA.2018.02.010.

Mao, Y., Park, T.J., Zhang, F., Zhou, H., Wong, S.S., 2007. Environmentally friendly methodologies of nanostructure synthesis. Small 3, 1122–1139. https://doi.org/10.1002/SMLL.200700048.

Matongo, S., Birungi, G., Moodley, B., Ndungu, P., 2015. Occurrence of selected pharmaceuticals in water and sediment of Umgeni River, KwaZulu-Natal, South Africa. Environ. Sci. Pollut. Res. Int. 22, 10298–10308. https://doi.org/10.1007/S11356-015-4217-0.

Mohamed, M.A.A., Carrasco-Marín, F., Elessawy, N.A., Hamad, H.A.F., 2020. Glucose-derived N-doped graphitic carbon: facile one-pot graphitic structure-controlled chemical synthesis with comprehensive insight into the controlling mechanisms. ChemistrySelect 5, 14685–14702. https://doi.org/10.1002/slct.202003014.

Munir Sajid, M., Zhai, H., Iqbal, M.A., Akhtar Shad, N., Javed, Y., Raza Ishaq, A., Abd Alreda, B., Morsy, K., Choi, J.R., 2023. Experimental insights on the synthesis and characteristics of Fe1−xBixVO4 photocatalysts for efficient environmental and electrical applications. Arab. J. Chem. 16, 104986 https://doi.org/10.1016/J.ARABJC.2023.104986.

Ng, Y.H., Iwase, A., Kudo, A., Amal, R., 2010. Reducing graphene oxide on a visible-light BiVO 4 photocatalyst for an enhanced photoelectrochemical water splitting. J. Phys. Chem. Lett. 1, 2607–2612. https://doi.org/10.1021/jz100978u.

Oliveira, T.S., Murphy, M., Mendola, N., Wong, V., Carlson, D., Waring, L., 2015. Characterization of Pharmaceuticals and Personal Care products in hospital effluent and waste water influent/effluent by direct-injection LC-MS-MS. Sci. Total Environ. 518–519, 459–478. https://doi.org/10.1016/J.SCITOTENV.2015.02.104.

Peña-Guzmán, C., Ulloa-Sánchez, S., Mora, K., Helena-Bustos, R., Lopez-Barrera, E., Alvarez, J., Rodriguez-Pinzón, M., 2019. Emerging pollutants in the urban water cycle in Latin America: a review of the current literature. J. Environ. Manag. 237, 408–423. https://doi.org/10.1016/J.JENVMAN.2019.02.100.

Quadra, G.R., Oliveira de Souza, H., Costa, R., dos, S., Fernandez, M.A., dos, S., 2016. Do pharmaceuticals reach and affect the aquatic ecosystems in Brazil? A critical review of current studies in a developing country. Environmental Science and Pollution Research 2016 24 (2 24), 1200–1218. https://doi.org/10.1007/S11356-016-7789-4.

Regmi, C., Dhakal, D., Lee, S.W., 2018. Visible-light-induced Ag/BiVO4 semiconductor with enhanced photocatalytic and antibacterial performance. Nanotechnology 29, 064001. https://doi.org/10.1088/1361-6528/AAA052.

Sajid, M.M., Shad, N.A., Javed, Y., Khan, S.B., Zhang, Z., Amin, N., Zhai, H., 2020. Preparation and characterization of Vanadium pentoxide (V2O5) for photocatalytic degradation of monoazo and diazo dyes. Surface. Interfac. 19, 100502 https://doi.org/10.1016/J.SURFIN.2020.100502.

Sajid, M.M., Zhai, H., Shad, N.A., Shafique, M., Afzal, A.M., Javed, Y., Khan, S.B., Amin, N., Zhang, Z., 2021. Construction of 1T-MoS2 quantum dots-interspersed (Bi1−xFex)VO4 heterostructures for electron transport and photocatalytic properties. RSC Adv. 11, 13105–13118. https://doi.org/10.1039/D1RA00807B.

Santos, L.H.M.L.M., Gros, M., Rodriguez-Mozaz, S., Delerue-Matos, C., Pena, A., Barceló, D., Montenegro, M.C.B.S.M., 2013. Contribution of hospital effluents to the load of pharmaceuticals in urban wastewaters: identification of ecologically relevant pharmaceuticals. Sci. Total Environ. https://doi.org/10.1016/j.scitotenv.2013.04.077.

Sarker, P., Lei, X., Taylor, K., Holmes, W., Yan, H., Cao, D., Zappi, M.E., Dianchen Gang, D., 2023. Evaluation of the adsorption of sulfamethoxazole (SMX) within aqueous influents onto customized ordered mesoporous carbon (OMC) adsorbents: performance and elucidation of key adsorption mechanisms. Chem. Eng. J. 454, 1385–8947. https://doi.org/10.1016/j.cej.2022.140082.

Sim, W.J., Lee, J.W., Lee, E.S., Shin, S.K., Hwang, S.R., Oh, J.E., 2011. Occurrence and distribution of pharmaceuticals in wastewater from households, livestock farms, hospitals and pharmaceutical manufactures. Chemosphere 82, 179–186. https://doi.org/10.1016/J.CHEMOSPHERE.2010.10.026.

Stathi, P., Solakidou, M., Deligiannakis, Y., 2021. Lattice defects engineering in W-, Zr-doped BiVO4 by flame spray pyrolysis: enhancing photocatalytic O2 evolution. Nanomaterials 2021 11. https://doi.org/10.3390/NANO11020501, 501 11, 501.

Subedi, B., Balakrishna, K., Joshua, D.I., Kannan, K., 2017. Mass loading and removal of pharmaceuticals and personal care products including psychoactives, antihypertensives, and antibiotics in two sewage treatment plants in southern India. Chemosphere 167, 429–437. https://doi.org/10.1016/J.CHEMOSPHERE.2016.10.026.

Thomaidis, N.S., Gago-Ferrero, P., Ort, C., Maragou, N.C., Alygizakis, N.A., Borova, V.L., Dasenaki, M.E., 2016. Reflection of cocioeconomic changes in wastewater: licit and illicit drug use patterns. In: Environmental Science and Technology, vol. 50. JPEG, pp. 10065–10072. https://doi.org/10.1021/ACS.EST.6B02417/ASSET/IMAGES/LARGE/ES-2016-02417Y_0001.

Tokunaga, S., Kato, H., Kudo, A., 2001. Selective preparation of monoclinic and tetragonal BiVO4 with scheelite structure and their photocatalytic properties. Chemistry of Materials 13, 4624–4628. https://doi.org/10.1021/cm0103390.

United Nations, 2017. World water development report, wastewater: the untapped resource. J. Chem. Inf. Model. 53, 1689–1699.

Van Boeckel, T.P., Gandra, S., Ashok, A., Caudron, Q., Grenfell, B.T., Levin, S.A., Laxminarayan, R., 2014. Global antibiotic consumption 2000 to 2010: an analysis of national pharmaceutical sales data. Lancet Infect. Dis. 14, 742–750. https://doi.org/10.1016/S1473-3099(14)70780-7.

Vergili, I., Kaya, Y., Gönder, Z.B., Boergers, A., Tuerk, J., 2019. Occurrence and prioritization of pharmaceutical active compounds in domestic/municipal wastewater treatment plants. Bull. Environ. Contam. Toxicol. 102, 252–258. https://doi.org/10.1007/s00128-019-02550-z.

Wang, H., Zhang, L., Chen, Z., Hu, J., Li, S., Wang, Z., Liu, J., Wang, X., 2014. Semiconductor heterojunction photocatalysts: design, construction, and photocatalytic performances. Chem. Soc. Rev. 43, 5234–5244. https://doi.org/10.1039/C4CS00126E.

Wang, Y., Hu, G., Cao, Y., Peng, Z., Du, K., 2021. One-pot synthesis of pre-reduced graphene oxide for efficient production of high-quality reduced graphene oxide and its lithium storage application. Mater. Chem. Phys. 265 https://doi.org/10.1016/J.MATCHEMPHYS.2021.124523.

Xie, S., Zhai, T., Zhu, Y., Li, W., Qiu, R., Tong, Y., Lu, X., 2014. NiO decorated Mo:BiVO4 photoanode with enhanced visible-light photoelectrochemical activity. Int. J. Hydrogen Energy 39, 4820–4827. https://doi.org/10.1016/J.IJHYDENE.2014.01.072.

Yan, Y., Sun, S., Song, Y., Yan, X., Guan, W., Liu, X., Shi, W., 2013. Microwave-assisted in situ synthesis of reduced graphene oxide-BiVO4 composite photocatalysts and their enhanced photocatalytic performance for the degradation of ciprofloxacin. J. Hazard Mater. 106–114. https://doi.org/10.1016/J.JHAZMAT.2013.01.051, 250–251.

Yang, L., Kruse, B., 2004. Revised Kubelka-Munk theory. I. Theory and application. J. Opt. Soc. Am.: Optics and Image Science, and Vision 21, 1933–1941. https://doi.org/10.1364/JOSAA.21.001933.

Zhai, H., Qi, J., Tan, Y., Yang, L., Li, H., Kang, Y., Liu, H., Shang, J., Park, H.S., 2020. Construction of 1D-MoS2 nanorods/LiNb3O8 heterostructure for enhanced hydrogen evolution. Appl. Mater. Today 18, 100536. https://doi.org/10.1016/J.APMT.2019.100536.

Zhang, J., Vasei, M., Sang, Y., Liu, H., Claverie, J.P., 2016. TiO2@Carbon photocatalysts: the effect of carbon thickness on catalysis. ACS Appl. Mater. Interfaces 8, 1903–1912. https://doi.org/10.1021/ACSAMI.5B10025/SUPPL_FILE/AM5B10025_SI_001.PDF.

Zhang, N., Zhang, Y., Xu, Y.J., 2012. Recent progress on graphene-based photocatalysts: current status and future perspectives. Nanoscale 4, 5792–5813. https://doi.org/10.1039/C2NR31480K.